

---

# PillarHist: A Quantization-aware Pillar Feature Encoder based on Height-aware Histogram

---

Sifan Zhou<sup>1†</sup>

Zhihang Yuan<sup>2†</sup>

Dawei Yang<sup>2◇</sup>

Xubin Wen<sup>1</sup>

Xing Hu<sup>2</sup>

Yuguang Shi<sup>1</sup>

Ziyu Zhao<sup>1</sup>

Xiaobo Lu<sup>1◇</sup>

<sup>1</sup>Southeast University

<sup>2</sup>Houmo AI

## Abstract

Real-time and high-performance 3D object detection plays a critical role in autonomous driving and robotics. Recent pillar-based 3D object detectors have gained significant attention due to their compact representation and low computational overhead, making them suitable for onboard deployment and quantization. However, existing pillar-based detectors still suffer from information loss along height dimension and large numerical distribution difference during pillar feature encoding (PFE), which severely limits their performance and quantization potential. To address above issue, we first unveil the importance of different input information during PFE and identify the height dimension as a key factor in enhancing 3D detection performance. Motivated by this observation, we propose a height-aware pillar feature encoder named PillarHist. Specifically, PillarHist statistics the discrete distribution of points at different heights within one pillar. This simple yet effective design greatly preserves the information along the height dimension while significantly reducing the computation overhead of the PFE. Meanwhile, PillarHist also constrains the arithmetic distribution of PFE input to a stable range, making it quantization-friendly. Notably, PillarHist operates exclusively within the PFE stage to enhance performance, enabling seamless integration into existing pillar-based methods without introducing complex operations. Extensive experiments show the effectiveness of PillarHist in terms of both efficiency and performance.

## 1 Introduction

LiDAR-based 3D object detection plays a pivotal role in various applications [42, 6, 54, 33, 10, 16], particularly in autonomous driving and robotics. It is important to detect the objects in the surrounding environment fastly and accurately, which places a high demand for both performance and latency. Existing mainstream methods can be categorized into two types based on the point cloud representation: (1) point-based [37, 29, 48, 9, 36] and (2) grid-based models [57, 47, 18, 7, 47, 25, 17]. Point-based models generally inherit the success in point cloud representation learning using deep neural networks[30, 51] and detect objects directly from raw points. However, these methods often face challenges in real-time onboard deployment as they often require point query/retrieval in 3D space ( *e.g.*, PointNet++ [31]). Grid-based methods rasterize the points into regular grid (voxel/pillar)

---

<sup>†</sup>Equal contribution

<sup>◇</sup>Corresponding author

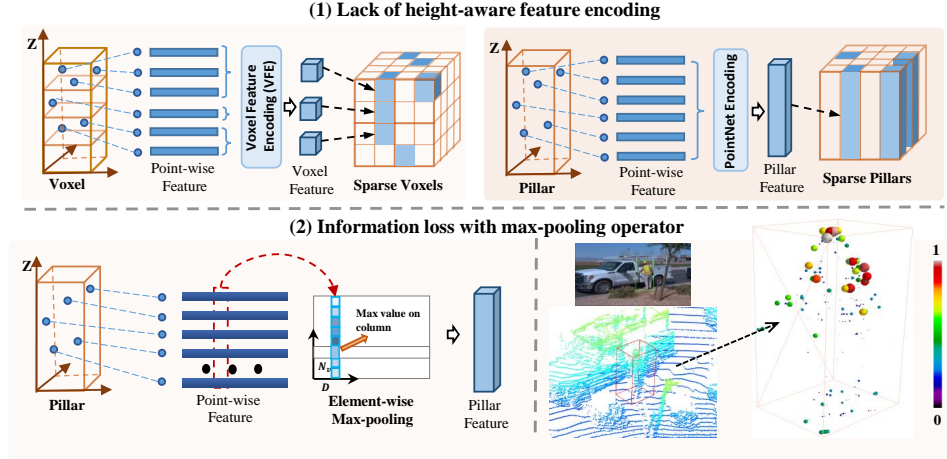


Figure 1: The drawbacks of pillar feature encoding are as follows: (1) Compared with the voxel feature encoding, the encoding process of pillars lacks height awareness, as it does not explicitly model the height dimension of the input point cloud. (2) PFE employs element-wise max-pooling operation, which inevitably results in information loss. As illustrated in the right side of (2), the max-pooling operation tends to preserve the feature information of points with higher height values within a pillar while disregarding points with lower height values, resulting in the loss of geometric information within the pillar.

and employ 2D or 3D convolution for feature learning. Compared to voxel-based methods, pillar-based detectors exhibit a more compact grid representation and can seamlessly integrate advanced 2D detection techniques without much modification. Therefore, those methods offer a favorable trade-off between performance and speed, making them highly suitable for practical deployment in autonomous systems. Furthermore, it is equally crucial to deploy them on resource-limited edge devices by improve their efficiency ( *e.g.*, reduce memory and computation cost).

The Pillar Feature Encoding (PFE) module plays a huge role in pillar-based networks [18, 50, 34, 19, 55]. Its main purpose is to transform the input point clouds, which are initially unordered ( $x, y, z$ , intensity) information, into pillars with a regular spatial arrangement. Each pillar has a fixed length of feature dimensions. In this paper, we observe that existing pillar-based methods suffer from two key problem in PFE module. ❶ Information loss significantly hampers their performance. ❷ Encoding scheme leads to a large variation of activations, making quantization challenging. As shown in Figure 1, the problem ❶ can be attributed to two factors: (1) **Lack of detailed height-aware feature encoding**. The height information is not well handled, resulting in an incomplete representation of the 3D scene. It is difficult to distinguish the height differences in various situations, like a pedestrian and a person standing on a car. (2) **Max-pooling operator causes the loss of height information**. The adoption of max-pooling operations within each pillar to derive pillar features leads to a loss of detailed information, which limits the ability of the encoded features to distinguish different objects.

The problem ❷ can be attributed the various arithmetic range of the PFE input. For instance, in nuScenes [2] dataset, the input of PFE includes  $\hat{p}_i = \{[x_i, y_i, z_i, r_i, x_i^m, y_i^m, z_i^m, x_i^c, y_i^c, z_i^c] \in \mathbb{R}^{N_v \times 10}\}$ , where  $[x_i, y_i, z_i] \in [-51.2, 51.2]$  is the point coordinates,  $r_i \in [0, 255]$  is the intensity,  $[x_i^m, y_i^m, z_i^m] \in [-0.2, 0.2]$  (pillar size = 0.2m) denotes the offset of  $[x_i, y_i, z_i]$  and the mean value of  $[x_i, y_i, z_i]$  within one pillar, and  $[x_i^c, y_i^c, z_i^c] \in [-4.0, 4.0]$  is the spatial offset of  $[x_i, y_i, z_i]$  and the pillar center. Details refer to Sec 3.1. The different part of input represents the global- and local-contextual information, but exhibit significant difference in numerical distribution. Therefore, the arithmetic disparity makes it more susceptible to the effects of quantization ( *e.g.*, clipping error).

To address the above issues, we propose a novel quantization-aware pillar feature encoder called PillarHist. It leverages a histogram technique to encode the height-aware information of each pillar into multiple bins, and the number of points falling within each bin is counted. The resulting histogram representation provides both semantic and geometric information from the height dimension. PillarHist incorporates the LiDAR reflection intensity of each point to obtain a weighted histogram of intensity, which adds distinguished height-aware information for object detection. These histograms, along with the pillar center coordinates, are concatenated and passed through a linear layer to obtain

a feature vector representing the pillar. Specially, PillarHist constrains the arithmetic distribution of PFE input to a stable range, making it friendly for further quantization. Besides, by operating linear projection at the pillar level instead of individual points, PillarHist significantly reduces the computation overhead, resulting in improved efficiency. It can be seamlessly integrated into existing pillar-based methods as a plugin module. Extensive experiments demonstrate the effectiveness of our proposed PillarHist in terms of both efficiency and performance. The contributions of our method can be summarised as follows:

- We conducted a thorough analysis of existing Pillar Feature Encoding (PFE) modules. Our findings indicate that they suffer from a loss of information in the height dimension and large variation of activation for quantization.
- We propose a novel PFE module called PillarHist, which can mitigate the height information loss and reduce the computation cost of PFE. It is noteworthy that we make it a plugin module to conveniently insert into existing mainstream pillar-based methods.
- We explore the quantization-friendly properties of PillarHist. PillarHist could effectively eliminate the severe performance degradation after quantization caused by the raw PFE, bringing quantization performance gain seamlessly.
- We conducted extensive experiments to evaluate the effectiveness of PillarHist. Our results showed that it achieved an average improvement of approximately 1.5% in Average Precision across various baselines.

In the following sections, we provide a detailed overview of related works in 3D object detection, and comprehensively describe our proposed PillarHist method. Subsequently, we present the experimental setup, evaluation results, and a thorough analysis of the obtained results. Finally, we conclude our paper and provide insights into potential future research directions of 3D object detection for autonomous driving and robotics.

## 2 Related Work

**Grid Feature Encoding.** Grid feature encoding is an essential module for grid-based 3D object detectors, and directly affects model’s accuracy[13, 24]. Several approaches have been proposed to extract features from two types of grid representations: Voxel and Pillar. VoxelNet [57] is a pioneering work that proposes a novel voxel feature encoding (VFE) layer to extract features. Many studies, including [58, 45, 53, 36, 41, 49, 44, 56], also adopt similar voxel encoding strategy. Similiar to voxel, pillars can be viewed as special voxels that do not have the vertical division. PointPillars [18] is a seminal work that leverages PointNet [30] for extracting point features within pillars and employs a maxpooling operator to obtain pillar features. Due to its compact representation, subsequent works [50, 43, 11, 34, 19, 55] have widely adopted the pillar representation following PointPillars [18]. PillarNet [34] designs a dynamic PFE module with less information loss, FastPillars [55] introduces a MAPE module with attentive-pooling to preserve more fine-grained geometrics. However, the PFE module in these methods do not explicitly consider the detailed height-aware information, and they all employ element-wise max-pooling or similar pooling operations, which still leading to information loss. In this paper, we focus on enhancing detailed height-aware information and mitigate the information loss caused by pooling operations.

**Quantization for 3D Object Detection.** With the wide application of 3D object detection in autonomous driving and robotics, some quantization methods are designed to improve inference speed for onboard deployment applications. With the advance of quantization techniques based on RGB image, QD-BEV [52] achieves smaller size and faster speed than baseline BevFormer [22] using Quantization-Aware Training (QAT) and distillation on multi-camera 3D detection tasks. For LiDAR-based 3D detection, [39] find that directly using INT8 quantization for 2D CNN will bring significant performance drop on PointPillars 18, where the reduction is even more severe for the entropy calibrator. Besides, BiPointNet [32] is a binarization quantization method, which focuses on classification and segmentation tasks based on point cloud captured from small CAD simulation. Recently, LiDAR-PTQ [54] unveils the root cause of performance collapse in the quantization of LiDAR-based detection and propose an effective PTQ method. However, some advanced quantization techniques[27, 21, 46, 23] are still required to find optimal quantization parameter in LiDAR-PTQ. Different with LiDAR-PTQ, which is a PTQ method tailored for point cloud detection, our PillarHist aim to make the distribution of weights as well as the processed data of an arbitrary distribution shall be quantization friendly.

### 3 Method

#### 3.1 Preliminary

**LiDAR-based 3D Object Detection.** We present the basic task definitions of LiDAR-based 3D object detection before introducing the detailed method. Given a point set with  $N$  points in the 3D space, which is defined as  $\mathbf{P} = \{\mathbf{p}_i = [x_i, y_i, z_i, r_i]^T \in \mathbb{R}^{N \times 4}\}$ , where  $x_i, y_i, z_i$  denote the coordinate values of each point along the axes X, Y, Z, respectively, and  $r_i$  is the LiDAR reflection intensity. Given a set of objects in the 3D scene  $\mathbf{B} = \{\mathbf{b}_j = [x_j, y_j, z_j, h_j, w_j, l_j, r_j, c_j]^T \in \mathbb{R}^{M \times 8}\}$ , where  $M$  is the total number of objects,  $b_i$  is the  $i$ -th object in the scene,  $x_j, y_j, z_j$  is the object’s center,  $h_j, w_j, l_j$  is the object’s size,  $r_j$  is the object’s heading angle and  $c_j$  is the object’s class. The task of 3D object detection is to predict the 3D bounding boxes  $\mathbf{B}$  from the point cloud  $\mathbf{P}$  in driving scenarios accurately.

**Point Cloud Pillarization.** Our aim is to transform the point cloud  $\mathbf{P}$  into a regular 3D pillar representation. Assuming that  $\mathbf{P}$  is in the 3D space with the range of  $L, W, H$  along the x, y, z axes, respectively, The point cloud  $\mathbf{P}$  is uniformly partitioned into a specific pillar grid of size  $(\delta_x, \delta_y, H)$ , we can compute the no-empty pillar index using:

$$(x_{int}, y_{int}, z_{int}) = (\lfloor \frac{x_i}{\delta_x} \rfloor, \lfloor \frac{y_i}{\delta_y} \rfloor, \lfloor \frac{H}{2} \rfloor), i = 0 \dots N - 1 \quad (1)$$

where  $\lfloor \cdot \rfloor$  is the floor operation,  $x_{int}, y_{int}, z_{int}$  is the 3D pillar index of  $p_i$  after pillarization. Notably, point cloud  $\mathbf{P}$  is only pillarized along the XY plane without the height dimension. Let  $V = \{v_i = [x_i, y_i, z_i, r_i] \in \mathbb{R}^{N_v \times 4}\}, i \in \{1, \dots, N_v\}$ , be a non-empty pillar contains  $N_v$  points,  $N_v$  is number of points in pillar  $V$ .

**Pillar Feature Encoding.** Pillar Feature Encoding (PFE) plays a crucial role in pillar-based 3D detection methods[18, 34, 55], directly impacting the representation learning of BEV feature and final detection accuracy. Here, taking PointPillars[18] as an example, we illustrate the details of PFE. **Firstly**, the points in each pillar are initially concatenated along the channel dimension to form  $\hat{p}_i = \{[x_i, y_i, z_i, r_i, x_i^m, y_i^m, z_i^m, x_i^c, y_i^c, z_i^c] \in \mathbb{R}^{N_v \times 10}\}$ , where  $[x_i, y_i, z_i]$  is the original point coordinates in the ego frame,  $[x_i^m, y_i^m, z_i^m]$  denotes the offset of  $p_i$  from the mean of the xyz coordinates of all points within the current pillar, and  $[x_i^c, y_i^c, z_i^c]$  is the offset of  $p_i$  from the current pillar center. Notably, for each pillar, a sampling or padding strategy is employed to ensure that all pillars contain the same number of points. **Secondly**, the concatenated point-wise features  $\hat{p}_i$  within a non-empty pillar  $V$  are mapped to the high-dimensional feature space using MLP layers. This process can be mathematically formulated as:

$$p_i^c = m(\hat{p}_i; w_m) \quad (2)$$

where the function  $m(\cdot)$  denotes MLP,  $w_m$  denotes the learnable weights of  $m(\cdot)$ , and  $p_i^c \in \mathbb{R}^{N_v \times D}$  is the point-wise feature. **Thirdly**, an element-wise max-pooling operation is applied along the dimension of point features, which is formulated as:

$$f^m = \max(p_i^c) \quad (3)$$

where  $\max(\cdot)$  means the max-pooling operator, and  $f^m \in \mathbb{R}^D$  is the resulting feature vector to represent non-empty pillar  $V$ . **Finally**, a non-empty pillar  $V \in \mathbb{R}^{N_v \times 4}$  consisting of  $N_v$  points is encoded into a feature vector  $f^m \in \mathbb{R}^D$ .

#### 3.2 What Kind of Information Do We Need in PFE?

**(1) Height Information is More Important.** As aforementioned, the pioneering pillar-based method PointPillars[18] concatenates two extra relation information along the channel dimension of the raw point cloud, i.e.  $([x_i^m, y_i^m, z_i^m])$  and  $([x_i^c, y_i^c, z_i^c])$ . Here, we decouple the input information along the  $x, y$ , and  $z$  axes, respectively. aiming to explore their impact on the final 3D detection performance. As shown in Table 1, when we only input the information along the  $x$  axis ( $x_i, x_i^m, x_i^c$ ) or the information along the  $y$  axis ( $y_i, y_i^m, y_i^c$ ), there is a significant degradation in the final 3D detection performance, The former results in a large decrease of 22.48 mAP of  $3D_{R40}$  and 21.23 mAP of  $3D_{R11}$ , while the latter leads to a large decrease of 20.58 mAP of  $3D_{R40}$  and 19.47 mAP of  $3D_{R11}$ . However, when we only input the information along the  $z$  axis ( $z_i, z_i^m, z_i^c$ ), it also achieves comparable performance with the baseline. This indicates that in the pillar feature encoding process, the information along the  $z$  axis, *a.k.a* the height dimension, plays a key role in the final 3D detection performance.

Table 1: Ablation results of different input for PFE in PointPillars on the KITTI *val* set in  $AP_{3D}$  (R40) and  $AP_{3D}$  (R11) for car.

$(x_i, x_i^m, x_i^c)$	$(y_i, y_i^m, y_i^c)$	$(z_i, z_i^m, z_i^c)$	$3D_{R40}$			$3D_{R11}$				
			mAP	Easy	Mod.	Hard	mAP	Easy	Mod.	Hard
✓			57.50	67.98	53.30	51.24	58.20	67.94	53.82	52.85
	✓		59.40	69.85	55.45	52.89	59.96	69.41	56.17	54.31
		✓	<b>79.63</b>	86.68	77.62	74.59	<b>79.15</b>	86.67	76.49	74.28
<b>PointPillars</b>			79.98	87.08	77.90	74.97	79.43	86.25	76.76	75.02

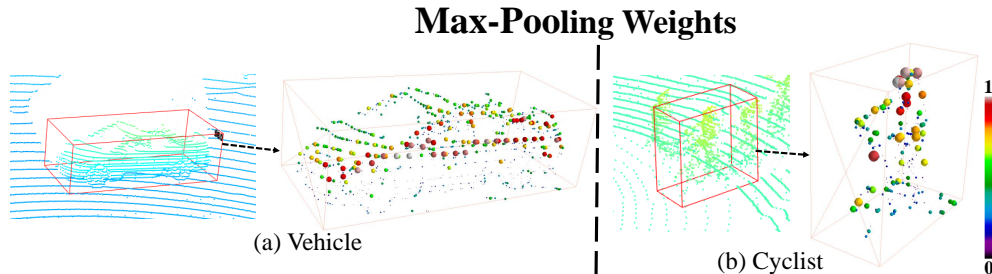


Figure 2: Visualization of the weights on (a) vehicle and (b) cyclist using Max-pooling in PFE. The size of points means scores. The point will be paid more attention if it has a higher score. Compared with original object’s points, max-pooling operator in PFE inevitably result in the loss of fine-grained information the object and local geometries. Best viewed in color.

**(2) Pillar Information Loss by Max-pooling.** As mentioned in the introduction (Section 1), current pillar-based methods [18, 50, 34, 55] heavily rely on max pooling to aggregate point features within each pillar. However, this max-pooling operation (as shown in Equation 3) inevitably leads to the loss of detailed information, particularly the local geometric patterns that play an important role in object recognition. To illustrate this point, we have visualized the effect of the max-pooling operation in Figure 2. In the figure, we represent the points that are more likely to be selected by max pooling as larger and red spheres. It is evident from the visualization that a significant number of points are not selected after the max-pooling operation, while only a small fraction of points have a high probability of being chosen. This comparison clearly demonstrates that the max-pooling operator results in a substantial loss of object geometry information compared to the original points of the object.

### 3.3 PillarHist: Height-aware Discrete Histogram for PFE

Hence, the challenge lies in finding a pillar encoding method that addresses these problems. Our goal is to develop a pillar encoding approach that possesses the following two key characteristics:

- ① It should eliminate the requirement for sampling operations while still maintaining the ability to capture the height-awareness of the points within each pillar. This means that the encoding method should effectively handle the variation in point density across different height levels within a pillar.
- ② It should keep the semantic and geometric information within the pillar, without resorting to max pooling or similar pooling operations. This is important to ensure that the encoded representation retains the relevant details and characteristics of the original pillar.

To achieve these objectives, we propose leveraging the histogram distribution. We can effectively capture the distribution of points within a pillar at different height levels. This allows us to maintain the height-awareness of the points without the need for sampling operations. The implementation of the histogram operation is straightforward. Initially, we divide the height range of the pillar into multiple bins, where each bin corresponds to a specific range of heights. For instance, if the pillar’s height spans from 0 to 10 meters, we can partition it into several bins such as 0-1m, 1-2m, 2-3m, and so forth. Next, we proceed to count the number of points that fall within each bin for a given pillar. This counting process yields a count value for each bin, indicating the number of points residing within that particular height range. For instance, if a larger number of points are found in the lower height range bins, it signifies a higher density of points near the bottom of the pillar. Conversely, if there is a greater concentration of points in the higher height range bins, it suggests a higher density of points towards the top of the pillar. This approach provides the model with both the semantic and

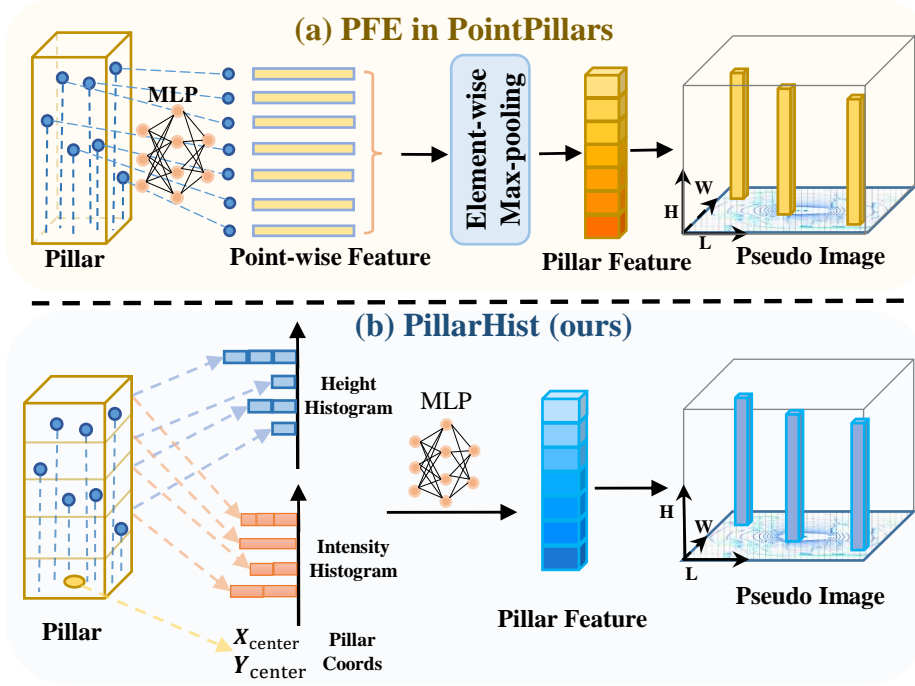


Figure 3: The overall architecture of our proposed PillarHist. The PFE (a) in PointPillars first extracts point-wise feature, and then the point-wise features are max-pooled along the point dimension to obtain the pillar-wise representation. This process has three key drawbacks: (1) it lacks detailed height-aware information, (2) the MLP operates on point-wise level, incurring computational burden, (3) the max-pooling operation leads to information loss. In contrast, our proposed PillarHist (b) directly encodes the height-aware information based on histogram, and then perform the MLP operation on the pillar level rather than point level. Finally, the max-pooling operation is also eliminated in proposed PillarHist.

---

**Algorithm 1** PillarHist for encoding the points in a pillar

---

**Input:** Raw point data in a pillar  $V \in \mathbb{R}^{N_v \times 4}$  consisting of  $N_v$  points, number of height bins  $B$ , number of output channels  $D$ , height of the pillar  $H$ , linear layer  $f_\theta$ .

**Output:** Pillar’s feature vector  $Y \in \mathbb{R}^D$  to represent the non-empty pillar  $V$ .

- 1: Divide the height  $H$  of the pillar into  $B$  bins, each bin having height  $h$ , where  $h = \frac{H}{B}$
  - 2: Initialize  $H^p \in \mathbb{R}^B$  to zero, where  $H^p$  represents the histogram of points in each bin
  - 3: Initialize  $H^i \in \mathbb{R}^B$  to zero, where  $H^i$  represents the weighted histogram of intensity in each bin
  - 4: **for**  $p_i = \{p_i | i = 1, 2, \dots, N_v\}$  **do**
  - 5:   Compute the corresponding bin index  $b_i$  based on the  $z$  coordinate  $z_i$  of point  $p_i$ :  $b_i = \lfloor \frac{z_i}{h} \rfloor$
  - 6:    $H^p[b_i] \leftarrow H^p[b_i] + 1$
  - 7:    $H^i[b_i] \leftarrow H^i[b_i] + r_i$   $\{r_i$  is the LiDAR reflection intensity of  $p_i\}$
  - 8: **end for**
  - 9:  $H^i[b_i] := H^i[b_i] / H^p[b_i]$  where  $H^i[b_i] \neq 0$
  - 10: Compute the pillar center coordinates  $x_{center}$  and  $y_{center}$
  - 11: Concatenate:  $[H^p | H^i | x_{center} | y_{center}] \in \mathbb{R}^{2B+2}$
  - 12: Linear projection:  $Y = f_\theta([H^p | H^i | x_{center} | y_{center}])$
- 

geometric information derived from the height dimension, thereby enhancing its understanding and representation of the point cloud data.

By using the histogram technique, we propose a height-aware pillar feature encoder named PillarHist. The algorithm is summarized in Algorithm 3: (1) We compute the histogram of each pillar, denoted as  $H^p \in \mathbb{R}^B$ , where  $B$  is the number of bins. (2) In addition, we incorporate the LiDAR reflection intensity of each point,  $r_i$ , to obtain the weighted histogram of intensity, denoted as  $H^i \in \mathbb{R}^B$ . The

weighted histogram represents the mean LiDAR reflection intensity for each bin, providing valuable height-aware information for object detection. **(3)** To provide the global position of each pillar, we utilize the x and y coordinates of the pillar center,  $x_{center}$  and  $y_{center}$ . Since the coordinates of the pillar are constant, this step does not require any additional computational effort. **(4)** We concatenate the computed histograms and the pillar center coordinates, resulting in  $[H^p|H^i|x_{center}|y_{center}] \in \mathbb{R}^{2B+2}$ . **(5)** To represent the features of the pillars, we utilize a linear layer  $f_\theta$  that projects the combined information into a feature vector.  $\theta \in \mathbb{R}^{D \times (2B+2)}$  and  $D$  is the number of output channels.

As shown in Fig 3, our PillarHist approach explicitly captures the histogram of points in different height intervals. This allows us to keep the semantic and geometric information within the pillar. PillarHist operates only during the PFE stage without introducing complex operations or interaction with other modules, allowing for seamless inserted into existing pillar-based methods serves as a plugin module with performance improvements.

**The efficiency of PillarHist:** **(1).** The linear projection in PillarHist operates on the pillar level, not on individual points. In contrast, the previous approach performed the linear projection for each point within a pillar. By employing the linear projection at the pillar level, we significantly decrease the number of floating-point operations (FLOPs) required by the PFE, resulting in improved efficiency. **(2).** PillarHist also avoids various memory-intensive operations, such as copying the original point cloud data, calculating distances  $(x^m, y^m, z^m, x^c, y^c, z^c)$ , and performing max pooling. This further enhances the efficiency of PillarHist in real-world deployment.

## 4 Experiments

We conduct extensive experiments on KITTI[12] and large-scale nuScenes[2] dataset. More dataset and implementation details refer to Appendix.

### 4.1 Overall Results

To evaluate the effectiveness and generalization ability of our proposed PillarHist, we use three popular pillar-based 3D detectors, PointPillars [18], Center-Point-Pillar [50], and PillarNet [34], as our baseline models.

Table 2: Performance of 3D object detection methods on nuScenes *test* set. <sup>†</sup> means the method that uses double-flip testing. All models listed take LIDAR data as input without image fusion or any model ensemble.

Method	NDS	mAP	Latency	Car	Truck	Bus	Trailer	C.V.	Ped.	Mot	Byc	T.C.	Bar
PointPillars [18]	45.3	30.5	31 ms	68.4	23.0	28.2	23.4	4.1	59.7	27.4	1.1	30.8	38.9
3DSSD [48]	56.4	42.6	-	81.2	47.2	61.4	30.5	12.6	70.2	36.0	8.6	31.1	47.9
CGBS [58]	63.3	52.8	80 ms	81.1	48.5	54.9	42.9	10.5	80.1	51.5	22.3	70.9	65.7
CVCNet [3]	64.2	55.8	122 ms	82.6	49.5	59.4	51.1	16.2	83.0	61.8	38.8	69.7	69.7
CenterPoint [50]	65.5	58.0	96 ms	84.6	51.0	60.2	53.2	17.5	83.4	53.7	28.7	76.7	70.9
HotSpotNet [4]	66.0	59.3	-	83.1	50.9	56.4	53.3	23.0	81.3	63.5	36.6	73.0	71.6
AFDetV2 [14]	68.5	62.4	-	86.3	54.2	62.5	58.9	26.7	85.8	63.8	34.3	80.1	71.0
UVTR-L [20] <sup>†</sup>	69.7	63.9	132 ms	86.3	52.2	62.8	59.7	33.7	84.5	68.8	41.1	74.7	74.9
VISTA [8] <sup>†</sup>	69.8	63.0	94 ms	84.4	55.1	63.7	54.2	25.1	82.8	70.0	45.4	78.5	71.4
Focals Conv[5]	70.0	63.8	138 ms	86.7	56.3	67.7	59.5	23.8	87.5	64.5	36.3	81.4	74.1
VoxelNeXt[6]	70.0	64.5	66 ms	84.6	53.0	64.7	55.8	28.7	85.8	73.2	45.7	79.0	74.6
PillarNet-18[34] <sup>†</sup>	70.8	65.0	78 ms	87.4	56.7	60.9	61.8	30.4	87.2	67.4	40.3	82.1	76.0
<b>PH-PillarNet-18<sup>†</sup></b>	<b>71.5</b>	<b>65.2</b>	73 ms	87.6	57.0	60.8	62.0	30.6	87.3	68.1	40.3	81.9	76.2

**Results on nuScenes Dataset.** The quantitative results on nuScenes *test* set are shown in Table 2. It can be seen that by integrating our proposed PillarHist into the current state-of-the-art pillar-based detector PillarNet [34] ( *e.g.*, PH-PillarHist), the proposed PH-PillarHist outperforms other approaches and achieves state-of-the-art performance on nuScenes test set, increasing 0.7 NDS and 0.2 mAP, respectively. Meanwhile, PH-PillarHist brings 5ms reduction on inference latency (78ms  $\rightarrow$  73ms). This presents the effectiveness and efficiency of PillarHist in not only boosting the detection accuracy, but also improving the computational efficiency, making it practical for real-world application.

**Generalization and Quantization Results.** Here, we conducted generalization and quantization experiments on different pillar-based baselines. **Firstly**, we selected three representative pillar-based detectors: PointPillars [18], CP-Pillar [50], and PillarNet [34]. In detail, we replace the raw PFE module in each baseline model with our proposed PillarHist, resulting in PH-PointPillars, PH-CP-Pillar, and PH-PillarNet, respectively. As shown in Table 3, the results demonstrate the

Table 3: Generalization and quantization performance comparison on nuScene *val* set.

Models	Bits (W/A)	NDS $\uparrow$	mAP $\uparrow$	mATE $\downarrow$	mASE $\downarrow$	mAOE $\downarrow$	mAVE $\downarrow$	mAAE $\downarrow$
PointPillars [18]	32/32	52.1	37.4	0.374	0.266	0.407	0.410	0.202
	8/8	44.8	29.8	0.526	0.287	0.391	0.596	0.208
<b>PH-PointPillars</b>	32/32	<b>53.8 (+1.7)</b>	38.8 (+1.4)	0.366	0.262	0.387	0.337	0.204
	8/8	<b>52.2(+7.4)</b>	37.0 (+7.2)	0.389	0.271	0.398	0.359	0.209
CP-Pillar[50]	32/32	56.4	44.9	0.336	0.266	0.532	0.289	0.189
	8/8	48.6	36.2	0.489	0.293	0.574	0.392	0.203
<b>PH-CP-Pillar</b>	32/32	<b>57.8 (+1.4)</b>	45.8 (+0.9)	0.330	0.264	0.514	0.215	0.188
	8/8	<b>56.3(+7.7)</b>	44.3 (+7.9)	0.344	0.269	0.551	0.238	0.195
PillarNet[34]	32/32	61.4	52.6	0.296	0.262	0.502	0.250	0.186
	8/8	54.6	43.1	0.392	0.268	0.510	0.338	0.194
<b>PH-PillarNet</b>	32/32	<b>63.0 (+1.6)</b>	52.7 (+0.1)	0.296	0.256	0.376	0.217	0.182
	8/8	<b>61.6(+7.0)</b>	51.4 (+8.3)	0.313	0.260	0.395	0.249	0.190

generalizability of proposed PillarHist, as we observe performance improvements of 1.7 NDS, 1.4 NDS, and 1.6 NDS on the three models, respectively. These results highlight the effectiveness and broad applicability of our PillarHist module in enhancing the representation power of pillar-based 3D object detectors, leading to consistent performance gains across different baseline architectures. **Secondly**, we conducted quantization experiments on above baseline models (refer to appendix for more quantization details). Specifically, we converted the weights and activations of the models from floating-point 32-bit to integer 8-bit and applied a simple post-training quantization setting to compress. As shown in Table 3, we found that the PointPillars, CP-Pillar, and PillarNet models suffered significant performance degradation after weight and activation quantization, with drops of 7.3 NDS and 7.6 mAP for PointPillars, 7.8 NDS and 8.7 mAP for CP-Pillar, and 6.8 NDS and 9.5 mAP for PillarNet. In contrast, the PH-PointPillars, PH-CP-Pillar, and PH-PillarNet models that integrate PillarHist only perform performance drops of 1.6 NDS, 1.5 NDS, and 1.4 NDS, respectively. Notably, the quantized models with PillarHist integration achieved comparable performance to original floating-point counterparts without PillarHist. These results demonstrate the quantization-friendly nature of PillarHist, which maintains the model’s representation power and performance even under quantization compression. This property is particularly valuable and practicable for deploying high-performance 3D object detectors on resource-constrained edge devices, where accuracy and latency are critical factors.

## 4.2 Ablation Study

Table 4: Performance of different PFE modules on the KITTI *val* set in AP<sub>3D</sub> (R40).

PFE module	Car 3D <sub>R40</sub>				Ped 3D <sub>R40</sub>				PFE GFLOPs
	mAP	Easy	<b>Mod.</b>	Hard	mAP	Easy	<b>Mod.</b>	Hard	
PFE[18]	79.98	87.08	77.90	74.97	49.41	54.71	49.01	44.52	0.152
DynPFE[50]	80.46	87.86	78.16	75.38	47.77	52.28	47.53	43.52	0.112
DynPFE*[34]	79.96	87.63	77.70	74.55	49.36	54.27	49.01	44.81	0.013
MAPE[55]	81.19	89.39	78.57	75.63	48.18	52.68	48.02	43.83	0.165
<b>PillarHist</b>	<b>81.42</b>	88.80	<b>79.13</b>	76.30	<b>51.07</b>	57.45	<b>50.42</b>	45.36	0.065

**Comparison of different PFE modules.** We compare the computation efficiency and performance of existing PFE modules. Specifically, we evaluate the following PFE modules: PFE in PointPillars [18], DynPFE in CenterPoint-Pillar [50], DynPFE in PillarNet [34] (denoted as DynPFE\*), and MAPE in FastPillars [55]. To ensure a fair comparison, we select PointPillars as the baseline method and conduct experiments by replacing the PFE module in PointPillars with other PFE module (DynPFE, DynPFE\*, MAPE and our PillarHist). This setting eliminates the performance difference caused by different backbone and regression heads. As shown in Table 4, our PillarHist achieves the highest 3D AP compared to other PFE methods while maintaining superior computational efficiency. In comparison to the PFE in PointPillars [18], PillarHist demonstrates significant performance improvements of 1.44 and 1.66 for vehicle and pedestrian, respectively, while utilizing only approximately 40% of the computational cost in terms of GFLOPs. It is worth noting that although DynPFE\* used in PillarNet [34] has lower GFLOPs, it suffers from poor detection performance.

**The effects of different feature in PillarHist.** Here, we conduct ablation study to analyze the impact of different input information in PillarHist. As depicted in the first and second rows in Table 5, when we incorporate the intensity information of points into pillar feature, it leads to performance



Table 5: Ablation results of different input for PillarHist on the KITTI *val* set for car and pedestrian.

height	intensity	pillar coords	Car $3D_{R40}$				Ped $3D_{R40}$			
			mAP	Easy	Mod.	Hard	mAP	Easy	Mod.	Hard
✓			80.18	87.47	78.18	75.22	48.06	53.75	47.51	42.92
✓	✓		80.81	88.29	78.62	75.53	49.62	55.42	49.10	44.36
✓	✓	✓	<b>81.41</b>	88.80	<b>79.13</b>	76.30	<b>51.07</b>	57.45	<b>50.42</b>	45.36

improvements for both the vehicle and pedestrian categories. Particularly for the pedestrian, there are significant performance improvements of approximately 1.7, 1.6, and 1.6 points in average precision (AP) for the easy, moderate, and hard levels, respectively. This notable improvement indicates that for small objects like pedestrians, the intensity values are crucial in distinguishing them from the background and enhancing their distinctive features. As shown in the second and third rows of the Table 5, by adding the pillar coordinates information, there is a performance improvement of 0.6 and 1.45 points in AP for the vehicle and pedestrian categories. We believe this improvement is because explicitly incorporating the global coordinate of the pillars during PFE helps the model better identify the object positions with the enhanced encoding information that includes height awareness. Notably, after adding the pillar coordinates, there is an improvement of 2.03 points in easy AP for pedestrians. This can be ascribed to the fact that the pillars encode not only varying height distribution information but also including the difference between empty and non-empty pillars.

Table 6: Ablation study on the number of bins  $s$  on the KITTI *val* set in  $AP_{3D}$  (R40).

bins	Car $3D_{R40}$				Ped $3D_{R40}$			
	mAP	Easy	Mod.	Hard	mAP	Easy	Mod.	Hard
$s=16$	80.27	87.57	78.15	75.10	45.79	50.35	45.62	41.41
$s=32$	80.49	87.98	78.28	75.22	49.79	55.35	49.48	44.56
$s=48$	81.24	89.31	78.69	75.74	50.08	55.42	49.91	44.93
$s=64$	<b>81.41</b>	88.80	<b>79.13</b>	76.30	<b>51.07</b>	57.45	<b>50.42</b>	45.36
$s=80$	80.49	87.53	78.44	75.50	49.96	55.82	49.68	44.38

**The number of Bins Along Height Dimension.** Here, we conduct an ablation study on the number of bins  $s$  in the height dimension. We take PointPillars as our baseline, Notably, PointPillars limits the maximum number of points as 32 in each pillar. We varied the number of bins from 16 to 80, and the results are presented in Table 6. As the number of bins increased, the performance of the model improved steadily. However, the performance did not exhibit a monotonic improvement trend and exhibited a degradation when the number of bins was increased to 80. Although larger number of bins can better encode discriminative features in the height dimension, the performance saturates when the number of bins becomes excessively large. Conversely, introducing too many parameters may pose additional optimization challenges, thereby hindering the model’s learning capacity. Based on these experimental results, we selected a value of 64 for the number of bins.

## 5 Limitation and Discussion

In this paper, we aim to introduce crucial height information into the PFE in pillar-based detectors, which inherently lacks the representation of height-aware information. While PillarHist focuses on enhancing the pillar feature representation, other dimensions and their interactions could also be explored to enhance the discriminative power of the features. Besides, we also acknowledge that a potentially effective approach could be to apply PillarHist to voxel-based detectors as well. However, this is not the main focus of this paper. In the appendix, we also explore the application of PillarHist to voxel-based methods. The experiments indicate that slightly performance gains. We think this is because the voxel has explicitly encoding the height information. Thereby the further height statistics within each voxel may not lead to significant benefits. Pleaser refer to appendix.

## 6 Conclusion

In this paper, we addressed the issue of information loss and large numerical distribution difference in existing pillar-based 3D object detectors during the PFE stage. We identify the height dimension as a crucial factor for enhancing 3D detection performance and proposed a height-aware pillar feature encoder called PillarHist. By leveraging a histogram technique, PillarHist preserved the information along the height dimension while effectively mitigating the information loss introduced by max-pooling operations. Importantly, PillarHist operated exclusively within the PFE stage, allowing

seamless insert into existing pillar-based methods serves as a plugin module. Meanwhile, PillarHist also constrains the arithmetic distribution of PFE input to a stable range, making it quantization-friendly. Extensive experiments demonstrated the effectiveness of PillarHist in terms of both efficiency and performance. Our proposed method achieved an average improvement of approximately 1.5% NDS across various baselines, showcasing its ability to enhance 3D object detection accuracy. The code for PillarHist will be released.

## References

- [1] Banner, R., Nahshan, Y., Soudry, D.: Post training 4-bit quantization of convolutional networks for rapid-deployment. *Advances in Neural Information Processing Systems* **32** (2019)
- [2] Caesar, H., Bankiti, V., Lang, A., Vora, S., Liong, V.E., Xu, Q., Krishnan, A., Pan, Y., Baldan, G., Beijbom, O.: Nuscenes: A multimodal dataset for autonomous driving. In: *CVPR*. pp. 11621–11631 (2020)
- [3] Chen, Q., Sun, L., Cheung, E., Jia, K., Yuille, A.: Every view counts: Cross-view consistency in 3d object detection with hybrid-cylindrical-spherical voxelization. *NeurIPS* (2020)
- [4] Chen, Q., Sun, L., Wang, Z., Jia, K., Yuille, A.: Object as hotspots: An anchor-free 3d object detection approach via firing of hotspots. In: *European conference on computer vision*. pp. 68–84. Springer (2020)
- [5] Chen, Y., Li, Y., Zhang, X., Sun, J., Jia, J.: Focal sparse convolutional networks for 3d object detection. In: *Proceedings of the IEEE Conference on Computer Vision and Pattern Recognition* (2022)
- [6] Chen, Y., Liu, J., Zhang, X., Qi, X., Jia, J.: Voxelnex: Fully sparse voxelnet for 3d object detection and tracking. In: *Proceedings of the IEEE/CVF Conference on Computer Vision and Pattern Recognition* (2023)
- [7] Deng, J., Shi, S., Li, P., Zhou, W., Zhang, Y., Li, H.: Voxel r-cnn: Towards high performance voxel-based 3D object detection. In: *AAAI* (2021)
- [8] Deng, S., Liang, Z., Sun, L., Jia, K.: Vista: Boosting 3d object detection via dual cross-view spatial attention. In: *Proceedings of the IEEE/CVF Conference on Computer Vision and Pattern Recognition*. pp. 8448–8457 (2022)
- [9] Fan, L., Wang, F., Wang, N., ZHANG, Z.X.: Fully sparse 3d object detection. *Advances in Neural Information Processing Systems* **35**, 351–363 (2022)
- [10] Fang, Z., Zhou, S., Cui, Y., Scherer, S.: 3d-siamrpn: An end-to-end learning method for real-time 3d single object tracking using raw point cloud. *IEEE Sensors Journal* **21**(4), 4995–5011 (2020)
- [11] Fu, J., Ren, G., Chen, Y., Liu, S.: Improved pillar with fine-grained feature for 3d object detection. *arXiv preprint arXiv:2110.06049* (2021)
- [12] Geiger, A., Lenz, P., Urtasun, R.: Are we ready for autonomous driving? the kitti vision benchmark suite. In: *2012 IEEE conference on computer vision and pattern recognition*. pp. 3354–3361. IEEE (2012)
- [13] Guo, Y., Wang, H., Hu, Q., Liu, H., Liu, L., Bennamoun, M.: Deep learning for 3d point clouds: A survey. *IEEE Transactions on Pattern Analysis and Machine Intelligence* **43**(12), 4338–4364 (2021). <https://doi.org/10.1109/TPAMI.2020.3005434>
- [14] Hu, Y., Ding, Z., Ge, R., Shao, W., Huang, L., Li, K., Liu, Q.: Afdetv2: Rethinking the necessity of the second stage for object detection from point clouds. In: *Proceedings of the AAAI Conference on Artificial Intelligence*. vol. 36, pp. 969–979 (2022)
- [15] Jeon, Y., Lee, C., Cho, E., Ro, Y.: Mr. biq: Post-training non-uniform quantization based on minimizing the reconstruction error. In: *Proceedings of the IEEE/CVF Conference on Computer Vision and Pattern Recognition*. pp. 12329–12338 (2022)

- [16] Jiayao, S., Zhou, S., Cui, Y., Fang, Z.: Real-time 3d single object tracking with transformer. *IEEE Transactions on Multimedia* (2022)
- [17] Kuang, H., Wang, B., An, J., Zhang, M., Zhang, Z.: Voxel-fpn: Multi-scale voxel feature aggregation for 3d object detection from lidar point clouds. *Sensors* **20**(3), 704 (2020)
- [18] Lang, A.H., Vora, S., Caesar, H., Zhou, L., Yang, J., Beijbom, O.: Pointpillars: Fast encoders for object detection from point clouds. In: *CVPR*. pp. 12697–12705 (2019)
- [19] Li, J., Luo, C., Yang, X.: Pillarnext: Rethinking network designs for 3d object detection in lidar point clouds. In: *IEEE/CVF Conference on Computer Vision and Pattern Recognition (CVPR)* (2023)
- [20] Li, Y., Chen, Y., Qi, X., Li, Z., Sun, J., Jia, J.: Unifying voxel-based representation with transformer for 3d object detection. In: *Advances in Neural Information Processing Systems* (2022)
- [21] Li, Y., Gong, R., Tan, X., Yang, Y., Hu, P., Zhang, Q., Yu, F., Wang, W., Gu, S.: Brecq: Pushing the limit of post-training quantization by block reconstruction. *arXiv preprint arXiv:2102.05426* (2021)
- [22] Li, Z., Wang, W., Li, H., Xie, E., Sima, C., Lu, T., Qiao, Y., Dai, J.: Bevformer: Learning bird’s-eye-view representation from multi-camera images via spatiotemporal transformers. In: *Computer Vision–ECCV 2022: 17th European Conference, Tel Aviv, Israel, October 23–27, 2022, Proceedings, Part IX*. pp. 1–18. Springer (2022)
- [23] Liu, J., Niu, L., Yuan, Z., Yang, D., Wang, X., Liu, W.: Pd-quant: Post-training quantization based on prediction difference metric. In: *Proceedings of the IEEE/CVF Conference on Computer Vision and Pattern Recognition*. pp. 24427–24437 (2023)
- [24] Mao, J., Shi, S., Wang, X., Li, H.: 3d object detection for autonomous driving: A comprehensive survey. *International Journal of Computer Vision* pp. 1–55 (2023)
- [25] Mao, J., Xue, Y., Niu, M., Bai, H., Feng, J., Liang, X., Xu, H., Xu, C.: Voxel transformer for 3d object detection. In: *ICCV*. pp. 3164–3173 (2021)
- [26] Migacz, S.: 8-bit inference with tensorrt. In: *GPU technology conference*. vol. 2, p. 5 (2017)
- [27] Nagel, M., Amjad, R.A., Van Baalen, M., Louizos, C., Blankevoort, T.: Up or down? adaptive rounding for post-training quantization. In: *International Conference on Machine Learning*. pp. 7197–7206. PMLR (2020)
- [28] Nagel, M., Fournarakis, M., Amjad, R.A., Bondarenko, Y., Van Baalen, M., Blankevoort, T.: A white paper on neural network quantization. *arXiv preprint arXiv:2106.08295* (2021)
- [29] Qi, C.R., Litany, O., He, K., Guibas, L.J.: Deep hough voting for 3D object detection in point clouds. In: *ICCV*. pp. 9277–9286 (2019)
- [30] Qi, C.R., Su, H., Mo, K., Guibas, L.J.: Pointnet: Deep learning on point sets for 3D classification and segmentation. In: *CVPR*. pp. 652–660 (2017)
- [31] Qi, C.R., Yi, L., Su, H., Guibas, L.J.: Pointnet++: Deep hierarchical feature learning on point sets in a metric space. In: *NeurIPS*. pp. 5099–5108 (2017)
- [32] Qin, H., Cai, Z., Zhang, M., Ding, Y., Zhao, H., Yi, S., Liu, X., Su, H.: Bipointnet: Binary neural network for point clouds. In: *ICLR* (2021)
- [33] Shan, J., Zhou, S., Fang, Z., Cui, Y.: Ptt: Point-track-transformer module for 3d single object tracking in point clouds. In: *2021 IEEE/RSJ International Conference on Intelligent Robots and Systems (IROS)*. pp. 1310–1316. IEEE (2021)
- [34] Shi, G., Li, R., Ma, C.: Pillarnet: Real-time and high-performance pillar-based 3d object detection. In: *ECCV* (2022)

- [35] Shi, S., Wang, X., Li, H.: Pointcnn: 3D object proposal generation and detection from point cloud. In: CVPR. pp. 770–779 (2019)
- [36] Shi, S., Wang, Z., Shi, J., Wang, X., Li, H.: From points to parts: 3d object detection from point cloud with part-aware and part-aggregation network. IEEE T-PAMI (2020)
- [37] Shi, W., Rajkumar, R.: Point-gnn: Graph neural network for 3D object detection in a point cloud. In: CVPR. pp. 1711–1719 (2020)
- [38] Smith, L.N., Topin, N.: Super-convergence: Very fast training of neural networks using large learning rates. In: Artificial intelligence and machine learning for multi-domain operations applications. vol. 11006, pp. 369–386. SPIE (2019)
- [39] Stäcker, L., Fei, J., Heidenreich, P., Bonarens, F., Rambach, J., Stricker, D., Stiller, C.: Deployment of deep neural networks for object detection on edge ai devices with runtime optimization. In: Proceedings of the IEEE/CVF International Conference on Computer Vision Workshop. pp. 1015–1022 (2021)
- [40] Team, O.D.: OpenPCDet: An open-source toolbox for 3D object detection from point clouds. <https://github.com/open-mmlab/OpenPCDet> (2020)
- [41] Tian, Y., Huang, L., Yu, H., Wu, X., Li, X., Wang, K., Wang, Z., Wang, F.Y.: Context-aware dynamic feature extraction for 3d object detection in point clouds. IEEE Transactions on Intelligent Transportation Systems **23**(8), 10773–10785 (2021)
- [42] Tian, Z., Chu, X., Wang, X., Wei, X., Shen, C.: Fully convolutional one-stage 3d object detection on lidar range images. NeurIPS (2022)
- [43] Wang, C., Liu, Z.: Cafi-pillars: Infusing geometry priors for pillar-based 3d detectors through centroid-aware feature interaction. IEEE Transactions on Intelligent Vehicles pp. 1–10 (2023). <https://doi.org/10.1109/TIV.2023.3323377>
- [44] Wang, T., Zhu, X., Lin, D.: Reconfigurable voxels: A new representation for lidar-based point clouds. arXiv preprint arXiv:2004.02724 (2020)
- [45] Wang, Y., Solomon, J.M.: Object dgcnn: 3d object detection using dynamic graphs. NeurIPS (2021)
- [46] Wei, X., Gong, R., Li, Y., Liu, X., Yu, F.: Qdrop: Randomly dropping quantization for extremely low-bit post-training quantization. arXiv preprint arXiv:2203.05740 (2022)
- [47] Yan, Y., Mao, Y., Li, B.: Second: Sparsely embedded convolutional detection. Sensors **18**(10), 3337 (2018)
- [48] Yang, Z., Sun, Y., Liu, S., Jia, J.: 3dssd: Point-based 3D single stage object detector. In: CVPR. pp. 11040–11048 (2020)
- [49] Ye, M., Xu, S., Cao, T.: Hynet: Hybrid voxel network for lidar based 3d object detection. In: Proceedings of the IEEE/CVF conference on computer vision and pattern recognition. pp. 1631–1640 (2020)
- [50] Yin, T., Zhou, X., Krahenbuhl, P.: Center-based 3d object detection and tracking. In: CVPR. pp. 11784–11793 (2021)
- [51] Yin, T., Zhou, X., Krahenbuhl, P.: Centerpoint++ submission to the waymo real-time 3d detection challenge (2021), accessed: 2021-12-05
- [52] Zhang, Y., Dong, Z., Yang, H., Lu, M., Tseng, C.C., Guo, Y., Keutzer, K., Du, L., Zhang, S.: Qd-bev: Quantization-aware view-guided distillation for multi-view 3d object detection (2023)
- [53] Zheng, W., Tang, W., Chen, S., Jiang, L., Fu, C.W.: Cia-ssd: Confident iou-aware single-stage object detector from point cloud. In: AAAI (2021)

- [54] Zhou, S., Li, L., Zhang, X., Zhang, B., Bai, S., Sun, M., Zhao, Z., Lu, X., Chu, X.: Lidar-ptq: Post-training quantization for point cloud 3d object detection. International Conference on Learning Representations (ICLR) (2024)
- [55] Zhou, S., Tian, Z., Chu, X., Zhang, X., Zhang, B., Lu, X., Feng, C., Jie, Z., Chiang, P.Y., Ma, L.: Fastpillars: A deployment-friendly pillar-based 3d detector. arXiv preprint arXiv:2302.02367 (2023)
- [56] Zhou, Y., Sun, P., Zhang, Y., Anguelov, D., Gao, J., Ouyang, T., Guo, J., Ngiam, J., Vasudevan, V.: End-to-end multi-view fusion for 3d object detection in lidar point clouds. In: Conference on Robot Learning. pp. 923–932. PMLR (2020)
- [57] Zhou, Y., Tuzel, O.: Voxelnet: End-to-end learning for point cloud based 3D object detection. In: CVPR. pp. 4490–4499 (2018)
- [58] Zhu, B., Jiang, Z., Zhou, X., Li, Z., Yu, G.: Class-balanced grouping and sampling for point cloud 3d object detection. arXiv:1908.09492 (2019)

## A Appendix / supplemental material

In this appendix, we first introduce implementation details in Sec. A.1. We then include additional experimental results in Sec. A.2, and post-training quantization algorithm in Sec. A.3.

### A.1 Implementation Details

**KITTI Dataset.** The KITTI has 7481 training samples and 7518 test samples. The training samples are split into a *train* set with 3,717 samples and a *val* set with 3,769 samples following the common setting [35, 18, 57, 47]. The detected boxes are classified into three subsets: “Easy”, “Moderate” and “Hard” based on the levels of difficulty. We report Mean Average Precision (mAP).

**nuScenes Dataset.** The nuScenes [2] dataset contains 700 training scenes, 150 val scenes and 150 test scenes. Each frame is generated approximately 30K points by a 32 channels LiDAR sampled with 20Hz. It contains 40K annotated key-frames and 10 categories in total. We report nuScenes detection score (NDS) and mAP, where NDS is the main ranking metric.

**Training Details.** We utilize the Adam optimizer with one-cycle learning rate policy [38]. The initial learning rate is set to  $10e-4$  during training. The learning rate gradually increases to 0.001 in the first 50% epochs and then gradually decreases to  $10e-5$  for the remaining training process. We set the weight decay to 0.01 and the momentum to a range of 0.85 to 0.95. For data augmentation, the whole point cloud is flipped randomly along the X axis, randomly is rotated along the Z axis in the range  $[-\pi/4, \pi/4]$ , and globally is scaled by a random factor sampled from  $[0.95, 1.05]$ . Regarding the pillar size, network architecture and loss function, we directly follow the setting of the four well-known pillar-based 3D detectors. (*i.e.*, PointPillars [18], CenterPoint-Pillar [50], PillarNet [34], FastPillars [55]). Our experiments are executed on 4 Nvidia Tesla V100 GPUs. We adopt OpenPCDet [40] as the training framework and faithfully reproduced the different baseline methods based on the provided official setting on kitti and nuScenes dataset in the OpenPCDet [40].

**Quantization Details.** In nuScenes [2] dataset, we uniformly sample 64 frames point cloud data from the validation set as the calibration set. The calibration set proportions is **1.06%** (64/6019). We set the first and the last layer of the network to keep full precision. We do not consider using Int8 quantization in MLP within PillarHist/PFE, since the input is 3D coordinates. We execute all experiments on a single Nvidia Tesla V100 GPU.

### A.2 More Experiments.

Table 7: Comparison with the Pillar-based methods on the KITTI *val* set.

Methods	Car $3D_{R40}$				Ped $3D_{R40}$			
	mAP	Easy	Mod.	Hard	mAP	Easy	Mod.	Hard
PointPillars [18]	79.98	87.08	77.90	74.97	49.41	54.71	49.01	44.52
<b>PH-PointPillars</b>	81.41	88.80	79.13	76.30	51.07	57.45	50.42	45.36
↑	<b>1.43</b>	<b>1.72</b>	<b>1.23</b>	<b>1.33</b>	<b>1.66</b>	<b>2.74</b>	<b>1.41</b>	<b>0.84</b>
CP-Pillar [50]	77.01	84.70	74.46	71.89	42.91	45.74	42.93	39.76
<b>PH-CP-Pillar</b>	77.85	85.62	75.17	72.77	44.93	49.10	44.99	40.72
↑	<b>0.84</b>	<b>0.92</b>	<b>0.71</b>	<b>0.88</b>	<b>2.02</b>	<b>3.36</b>	<b>2.06</b>	<b>0.96</b>
PillarNet [34]	80.90	87.21	79.05	76.44	44.51	47.83	44.80	41.01
<b>PH-PillarNet</b>	81.60	88.71	79.05	77.03	46.10	49.75	45.96	42.61
↑	<b>0.70</b>	<b>1.50</b>	0.00	<b>0.59</b>	<b>1.62</b>	<b>1.92</b>	<b>1.16</b>	<b>1.60</b>

**Generalization of PillarHist for Other Pillar-based Detectors.** As shown in Table 7, when compared to pointpillars [18], CenterPoint-Pillar [50], and PillarNet [34] methods, our method achieves mAP improvements of 1.43, 0.84, and 0.70 for the vehicle class, respectively. For the pedestrian category, PillarHist achieves even larger performance gains of 1.66, 2.02, and 1.62 points on mAP, respectively. These improvements indicate that our histogram-based point feature encoder can generate more informative features to enhance object detection performance.

Table 8: The effects of PillarHist on SECOND[47] on the KITTI *val* set.

Methods	Car $3D_{R40}$				Ped $3D_{R40}$			
	mAP	Easy	Mod.	Hard	mAP	Easy	Mod.	Hard
SECOND [47]	83.59	90.55	81.61	78.60	51.08	55.94	51.14	46.17
<b>PH-SECOND</b>	83.96	91.04	81.95	78.90	51.41	56.38	51.82	46.03
↑	<b>0.37</b>	<b>0.49</b>	<b>0.34</b>	<b>0.30</b>	<b>0.33</b>	<b>0.44</b>	<b>0.68</b>	-

**The Effects of PillarHist on Voxel-based Detectors.** As shown in Table 8, we integrate PillarHist into SECOND [47], a representative voxel-based 3D object detector. The results demonstrate that the proposed PillarHist can still lead to performance improvements for voxel-based methods, albeit with slight margin compared to the gains observed for pillar-based detectors. We conjecture that this can

be attributed to the inherent design of voxel-based methods. Specifically, voxel-based approaches explicitly encode height information by discretizing the input point cloud into voxel features along the height dimension, which are then processed using 3D CNN. Therefore, further encoding finer-grained height statistics within each voxel may not yield substantial performance benefits due to the sparsity of point clouds, as the height-aware features are already captured by the underlying voxel representation.

Table 9: Ablation results of different input for PFE in PointPillars on the KITTI *val* set for car.

$(x_i, y_i, z_i)$	$(x_i^m, y_i^m, z_i^m)$	$(x_i^c, y_i^c, z_i^c)$	$3D_{R40}$				$3D_{R11}$			
			mAP	Easy	Mod.	Hard	mAP	Easy	Mod.	Hard
✓			79.08	86.20	77.07	73.98	78.38	86.06	76.47	72.61
	✓		63.44	75.51	58.59	56.21	62.64	73.50	58.20	56.22
		✓	<b>79.88</b>	87.06	77.80	74.79	<b>79.40</b>	86.27	77.06	74.87
<b>PointPillars</b>			79.98	87.08	77.90	74.97	79.43	86.25	76.76	75.02

**Local Relation Information is More Important.** As discussed in Sec 3, as  $([x_i^m, y_i^m, z_i^m])$  is obtained by subtracting the mean of the coordinates of all points within the current pillar from the coordinates of the current point, it represents the relative context of all points within the pillar in the global coordinate. Similarly,  $([x_i^c, y_i^c, z_i^c])$  is obtained by subtracting the center coordinates of the current pillar from the coordinates of the current point, it contains the relative context of all points within the pillar in the local coordinate system centered around the pillar’s center. Here, we first decouple these different input information along the channel dimension of the points and conduct ablation experiments to investigate their impact on the final 3D detection performance.

Table 10: Ablation results of different input for PFE with variant channel ratio on the KITTI *val* set for car.

Input	Channel Ratio	GFLOPs	$3D_{R40}$				$3D_{R11}$			
			mAP	Easy	Mod.	Hard	mAP	Easy	Mod.	Hard
PointPillars	1.0	63.30	79.98	87.08	77.90	74.97	79.43	86.25	76.76	75.02
$(x_i^c, y_i^c, z_i^c)$	0.5	16.25	78.05	86.93	75.23	71.99	77.39	85.78	75.42	70.97
	0.75	35.94	<b>79.90</b>	87.19	<b>77.76</b>	74.77	<b>79.17</b>	86.20	<b>76.86</b>	74.45
	1.0	60.25	79.88	87.06	77.80	74.79	79.40	86.27	77.06	74.87
$(z_i, z_i^m, z_i^c)$	0.5	16.25	79.18	87.66	76.99	72.91	78.26	86.80	76.45	71.54
	0.75	35.94	<b>79.55</b>	87.28	<b>77.46</b>	73.91	<b>78.67</b>	86.62	<b>76.61</b>	72.79
	1.0	60.25	79.63	86.68	77.62	74.59	79.15	86.67	76.49	74.28
PH-PointPillar	0.5	16.21	79.32	87.49	77.39	73.10	78.34	86.46	76.57	72.00
	0.75	35.90	<b>81.00</b>	88.07	<b>78.86</b>	75.97	<b>80.50</b>	87.84	<b>77.65</b>	76.00
	1.0	60.21	81.41	88.80	79.13	76.30	80.72	87.86	77.91	76.41

**Rethinking the Model Scale.** Based on the results in Table 1 and Table 9, we further argue whether the model still requires the original scale for feature learning, even after reducing the redundant input information in the PFE module. To explore this, we take PointPillars [18] as an example and scaled down both the baseline model and PH-PointPillars by ratios of 0.75 and 0.5, as shown in Table 10. Surprisingly, we found that even when the model’s input contained only height information or only local coordinate or height-aware and pillar coordinates (PillarHist), their performance did not exhibit significant degradation under the 0.5 ratio channel setting. Furthermore, under the 0.75 ratio channel setting, the models achieve comparable performance to the baseline model. This phenomenon prompts us to rethink whether there is still substantial redundancy in existing pillar-based detectors. We remain this issue as an open problem for future research and encourage the community to explore more compact and efficient detection models.

### A.3 Quantization Preliminaries

**Quantization for tensor.** The quantization operation is defined as the mapping of a floating-point (FP) value  $x$  (weights or activations) to an integer value  $x_{int}$  according to the following equation:

$$x_{int} = clamp(\lfloor \frac{x}{s} \rceil + z, q_{min}, q_{max}) \tag{4}$$

where  $\lfloor \cdot \rceil$  is the rounding-to-nearest operator, which results in the rounding error  $\Delta r$ . The function  $clamp(\cdot)$  clips the values that lie outside of the integer range  $[q_{min}, q_{max}]$ , incurring a clipping error  $\Delta c$ .  $x_{int}$  represents the quantized integer value.  $z$  is zero-point.  $s$  denotes the quantization scale factor, which reflects the proportional relationship between FP values and integers.  $[q_{min}, q_{max}]$  is

the quantization range determined by the bit-width  $b$ . Here, we adopt uniform signed symmetric quantization, as it is the most widely used in TensorRT [26] and brings significant acceleration effect. Therefore,  $q_{min} = -2^{b-1}$  and  $q_{max} = 2^{b-1} - 1$ . Nonuniform quantization [15] is challenging to deploy on hardware, so we disregard it in this work. Generally, weights can be quantized without any need for calibration data. Therefore, the quantization of weights is commonly solved using grid search or analytical approximations with closed-form solution [1, 28] to minimize the mean squared error (MSE) in PTQ. However, activation quantization is input-dependent, so often requires a few batches of calibration data for the estimation of the dynamic ranges to converge. To approximate the real-valued input  $x$ , we perform the de-quantization step:

$$\hat{x} = (x_{int} - z) \cdot s \quad (5)$$

where  $\hat{x}$  is the de-quantized FP value with an error that is introduced during the quantization process.

**Quantization range.** If we want to reduce clipping error  $\Delta c$ , we can increase the quantization scale factor  $s$  to expand the quantization range. However, increasing  $s$  leads to increased rounding error  $\Delta r$  because  $\Delta r$  lies in the range  $[-\frac{s}{2}, \frac{s}{2}]$ . Therefore, the key problem is how to choose the quantization range  $(x_{min}, x_{max})$  to achieve the right trade-off between clipping and rounding error. Specifically, when we set fixed bit-width  $b$ , the quantization scale factor  $s$  is determined by the quantization range:

$$s = (x_{max} - x_{min}) / (2^b - 1) \quad (6)$$

**Max-min calibration.** We can define the quantization range as:

$$x_{max} = \max(|x|), x_{min} = -x_{max} \quad (7)$$

to cover the whole dynamic range of the floating-point value  $x$ . This leads to no clipping error. However, this approach is sensitive to outliers as strong outliers may cause excessive rounding errors.

**Quantization for network.** For a float model with  $N$  layer, we primarily focus on the quantization of convolutional layers or linear layers, which mainly involves the handling of weights and activations. For a given layer  $L_i$ , we initially execute quantization operations on its weight and input tensor, as illustrated in Eq 9 and 5, yielding  $\hat{W}_i$  and  $\hat{I}_i$ . Consequently, the quantized output of this layer can be expressed as follows.

$$\hat{A}_i = f(BN(\hat{I}_i \otimes \hat{W}_i)) \quad (8)$$

where  $\otimes$  denotes the convolution operator,  $BN(\cdot)$  is the Batch-Normalization procedure, and  $f(\cdot)$  is the activation function. Quantization works generally take into account the convolution, Batch Normalization (BN), and activation layers.

**Grid Search for Weight and Activation Quantization Scale.** For a weight or activation tensor  $X$ , we can get their initial quantization scale factor using the following equation:

$$\hat{x} = (\text{clamp}(\lfloor \frac{x}{s} \rfloor + z, q_{min}, q_{max}) - z) \cdot s \quad (9)$$

$$s = (x_{max} - x_{min}) / (2^b - 1) \quad (10)$$

$$\operatorname{argmin}_{s_t} \left\| \left( X - \hat{X}(s_t) \right) \right\|_F^2 \quad (11)$$

$\|\cdot\|_F^2$  is the Frobenius norm (MSE Loss). Then linearly divide the interval  $[\alpha s_0, \beta s_0]$  into  $T$  candidate bins, denoted as  $\{s_t\}_{t=1}^T$ .  $\alpha$ ,  $\beta$  and  $T$  are designed to control the search range and granularity. Finally, search  $\{s_t\}_{t=1}^T$  to find the optimal  $s_{opt}$  that minimizes the quantization error, the grid search method in Algorithm2.

**Naive Post-Training Quantization Algorithm.** The naive post-training quantization algorithm is as follows, the grid search method in Algorithm3.



---

**Algorithm 2** Grid search

---

**Input:** the input of full precision tensor  $X$ , bit-width  $b$  and  $T$  bins.

**Output:** scale factor  $s_{opt}$  with  $\min(\|(X - \hat{X}(s_l))\|_F^2)$ .

- 1: using  $x_{max} = \max(|x|)$  get max value of tensor  $X$
  - 2: set  $range = x_{max}$ ,  $c_{best} = 100$
  - 3: set  $v_{min} = x_{min}$  and  $v_{max} = x_{max}$
  - 4: **for**  $i$  in range(1,  $T$ ) **do**
  - 5:    $threshold = range/T/i$
  - 6:    $x_{min} = -threshold$ ,  $x_{max} = threshold$
  - 7:   get scale  $s_t$  with  $x_{min}$  and  $x_{max}$  using Eq 10
  - 8:   input the quantized value  $\hat{x}$  and FP value  $x$  using Eq 9 to get score  $c$
  - 9:   update  $v_{min}$  and  $v_{max}$  when  $c < c_{best}$  and update  $c_{best} = c$
  - 10: **end for**
  - 11: get  $v_{min}$  and  $v_{max}$  with the minimal score  $c$
  - 12: get final scale  $s_{opt}$  with  $v_{min}$  and  $v_{max}$  using Eq 10
  - 13: **return** scale  $s_{opt}$
- 

---

**Algorithm 3** Naive Post-Training Quantization for PillarHist

---

**Input:** Pretrained FP model with  $N$  layers; Calibration dataset  $D^c$ .

**Output:** quantization parameters of both activation and weight in network, i.e., weight scale  $s_w$ , weight zero-point  $z_w$ , activation scale  $s_a$  and activation zero-point  $z_a$ .

- 1: Get only weight quantization parameters  $s_w$  and  $z_w$  to minimize Eq 11 in every layer using the grid search algorithm;
  - 2: **for**  $L_n = \{L_i | i = 1, 2, \dots, N\}$  **do**
  - 3:   Optimize only activation quantization parameters  $s_a$  and  $z_a$  to minimize Eq 11 in layer  $L_i$  using the grid search algorithm;
  - 4:   Quantize layer  $L_i$  with the quantization parameters  $s_w$ ,  $z_w$ ,  $s_a$ , and  $z_a$ ;
  - 5: **end for**
-